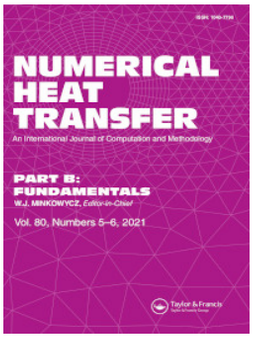

Taylor & Francis
Taylor & Francis Group

Numerical Heat Transfer, Part B: Fundamentals
An International Journal of Computation and Methodology

ISSN: (Print) (Online) Journal homepage: https://www.tandfonline.com/loi/unhb20

A simplified and efficient Gay-Lussac approach for non-Boussinesq treatment of natural convection problems

Peyman Mayeli & Gregory J. Sheard

To cite this article: Peyman Mayeli & Gregory J. Sheard (2021) A simplified and efficient Gay-Lussac approach for non-Boussinesq treatment of natural convection problems, Numerical Heat Transfer, Part B: Fundamentals, 80:5-6, 115-135, DOI: 10.1080/10407790.2021.1946310

To link to this article: https://doi.org/10.1080/10407790.2021.1946310

Published online: 06 Jul 2021.

Submit your article to this journal

Article views: 19

View related articles

View Crossmark data

Full Terms & Conditions of access and use can be found at
https://www.tandfonline.com/action/journalInformation?journalCode=unhb20

NUMERICAL HEAT TRANSFER, PART B: FUNDAMENTALS
2021, VOL. 80, NOS. 5–6, 115–135
https://doi.org/10.1080/10407790.2021.1946310

Taylor & Francis
Taylor & Francis Group

Check for updates

A simplified and efficient Gay-Lussac approach for non-Boussinesq treatment of natural convection problems

Peyman Mayeli and Gregory J. Sheard

Department of Mechanical and Aerospace Engineering, Monash University, Clayton, Victoria, Australia

ABSTRACT

Under the Boussinesq approximation for buoyancy driven flows, density variations are restricted to the gravity term. In contrast, the Gay-Lussac (GL) approach is developed based on considering density variations in any term of the Navier—Stokes equations in which density appears. In both incompressible approaches, a linear density state equation is adopted to relate density variations to temperature differences. In this article, a simplified Gay-Lussac (SGL) approach with a reduced computational cost is proposed in which density variations are omitted from the continuity equation. It is shown that the SGL approach gives identical results to the traditional GL approach in both transient and steady states. Then, performance of the SGL approach at high relative temperature differences up to $\varepsilon = 0.3$ is evaluated against the low Mach number scheme and the Boussinesq approximations. In this respect, natural convection in square cavity benchmark problem at three different inclination angles ($\gamma = 0$ and $\pm\pi/6$) is simulated up to $Ra = 10^7$ at $Pr = 1$ and results are analyzed in terms of the local and average Nusselt number, and the skin friction coefficient. Comparing computational cost of simulations at $Ra = 10^7$ indicates the introduced SGL approach has 17% and 11% less computational cost using upwind and central schemes, respectively, compared to the traditional GL approach, while the convergence rate is not affected by the proposed simplification. Comparing the Nusselt number shows a negligible difference between the SGL and the Boussinesq approximations at high relative temperature differences, both deviating from the low Mach number scheme. Finally, by comparing the friction coefficient results obtained by the SGL approach against the weakly compressible approach it is concluded that the GL family approaches require serious revisions to outperform the Boussinesq approximation as an incompressible approach for buoyancy driven flows with high relative temperature differences.

ARTICLE HISTORY
Received 14 April 2021
Accepted 17 June 2021

1. Introduction

The well-known Boussinesq approximation [1] is still the most common approach for the numerical simulation of natural convection (NC) problems. The general idea of treating natural convection (NC) as incompressible by ignoring density variations except in the buoyancy term first was proposed by Oberbeck [2], which is why the approximation's is sometimes referred to as the Oberbeck—Boussinesq (OB) approximation. Under the OB approximation, a linear state equation is adopted to relate density variations to temperature differences. The OB approximation due to its great accuracy of performance for problems associated by differential temperature differences

CONTACT Peyman Mayeli peyman.mayeli@gmail.com Department of Mechanical and Aerospace Engineering, Monash University, Room 354, Level 3, Woodside Building for Technology and Design, 20 Exhibition Walk, Clayton, VIC 3800 Australia.

© 2021 Taylor & Francis Group, LLC

Nomenclature

Be_{ave}	average Bejan number
c_f	skin friction coefficient
D	diffusion operator
e_g	unit vector in gravity direction
g	gravitational acceleration
Ga	Gay-Lussac number ($\beta\Delta\theta$)
L_{ref}	reference length
N	Nonlinear operator
Nu_{ave}	average Nusselt number
Nu_{loc}	local Nusselt number
p	pressure
p^*	modified pressure
P	dimensionless pressure
P_{th}	thermodynamic pressure
Pr	Prandtl number
R	ideal gas constant
Ra	Rayleigh number
S	surface
T	temperature
x	coordinate vector
X	dimensionless coordinate vector
u	velocity vector
U	dimensionless velocity vector
α	thermal diffusivity
β	isobaric expansion coefficient
γ	cavity inclination angle
ε	relative temperature difference
η	heat capacity ratio
θ	physical temperature
Θ	dimensionless temperature
μ	dynamic viscosity
ν	kinematic viscosity
ρ	density
ρ_0	reference density
τ_w	wall shear stress
ϕ	gravitational potential

Subscript

ave	average
c	cool
h	hot
loc	local
ref	reference
tot	total

has been used as the basis of many benchmark natural convection problems in different geometries such as rectangular [3–8], triangular [9–12] and annulus [13–15] enclosures.

One of the fundamental assumptions of the OB approximation is small temperature differences, which justifies restricting density variations to the buoyancy term. Indeed, applying the OB approximation on cases that are featuring large density variations produces inaccurate results [16]. Foundry processes, astrophysical magnetohydrodynamics [17], thermal insulation systems in nuclear reactors [18] and solar collectors [19–20] are samples that such a situation may take place. Numerical techniques that seek to circumvent the limitations of the OB approximation are less abundant in the literature. In general, non-OB approximations for NC problems occupy two general categories, compressible and incompressible.

The first category of the non-OB algorithms is developed by retaining compressibility within the Navier—Stokes equations, which leads to the introduction of the Mach number. This strategy is seldom used for numerical simulation of NC problems due to instability at small order of compressibility ratio for density-based compressible flow solvers; examples include Vierendeels *et al.* [21], Fu *et al.* [22], Busto *et al.* [23], and Bermúdez *et al.* [24]. Small orders of Mach umber in natural convection problems motivated the use of the low Mach number scheme (LMS). Under the this approximation developed by Paulucci [25], acoustic waves are removed from the governing equation and total pressure is split into two main parts a global (uniform) thermodynamic pressure which is obtained from the equation of state and used for updating the density variations through the solution procedure, and a local hydrodynamic pressure which acts in the momentum equations to establish a balance among advection, buoyancy, and diffusion terms. Vierendeels *et al.* [26] and Becker & Braack [27] applied this technique for numerical simulation of the square cavity benchmark problem with large temperature differences beyond the validity of the OB regime.

The second category of the non-OB approximations are developed under the fundamental assumption of incompressibility. One of the remedies to avoid the OB approximation in this

category is the Gay-Lussac (GL) approach, which is developed based on considering density variations beyond the gravity term. Under the GL approximation, buoyancy effects are taken into account wherever density appears in the governing equations. Such a strategy invokes the GL parameter as a product of the volumetric thermal expansion coefficient and the reference temperature difference ($Ga = \beta\Delta\theta$). Under the GL approach, a pre-factor of ($1 - Ga\Theta$) acts as a modifier on the aforementioned terms in dimensionless form of the governing equations. The strength of this pre-factor and its modification effects become more visible by increasing the GL parameter at high temperature differences. It can also be shown that governing equations under the GL approach recover the OB approximation as $Ga \to 0$. For instance, the square cavity benchmark problem with large density variations was analyzed under the GL approach by Pesso & Piva [28]. A GL-type approximation is also possible by extension of buoyancy effects to one of the advection or convection terms of the momentum and energy equations, respectively. In this category, a GL-type approach is proposed by Lopez *et al.* [29] in which density variations were extended only to the centrifugal part of the advection term to capture centrifugal effects arising from background rotation in those rapidly rotating flows. This approach continued by Mayeli & Sheard [30–31]. They showed that the GL parameter may be expressed in terms of the Rayleigh, Prandtl and Froude numbers ($Ga = RaPrFr$). Since the GL parameter appears in the dimensionless form of the linear density relation, a maximum value $Ga_{max} = 2$ should be considered to avoid an unphysical (negative) density. Such a constraint also confines the maximum physical value of the Froude number at each Rayleigh and Prandtl number to $2/RaPr$ ($Fr_{\max} = 2/RaPr$). Mayeli & Sheard [30–31] also established a relation for the GL-type family approach that matches the Froude number corresponding to a given relative temperature difference (ε) at each Ra and Pr as $Fr = 2\varepsilon/RaPr$.

Another incompressible-based strategy to go beyond the OB approximation is considering nonlinear terms via retention of higher terms (e.g. square and cubic terms) of the density state relation, that enables the non-OB category to a wider spectrum of temperature difference. A nonlinear density state relation may also justify strange behavior of some fluids at temperatures close or equal maximum density. For instance, the density-temperature relationship of cold water in the vicinity of 4 °C does not obey a linear function. In this situation, the linear density state relation may not be valid anymore even for small temperature differences within valid temperature difference range of the OB regime. For these types of problems, a dimensionless temperature known as the inversion parameter is defined which relates the temperature of the maximum density to the hot and cold reference temperatures. Since for inversion parameter values smaller than unity the temperature corresponding to the maximum density lies between the hot and cold reference temperatures, studies in this category are focused on this range and the corresponding flow patterns due to different inversion parameters. For instance, this strategy was used by Li *et al.* [32] for natural convection of water near its maximum density in an eccentric annulus cavity.

Under the OB approximation, dissipated heat due to viscous friction and work of pressure stress are removed from the energy equation as their effects are supposed to be negligible. Justification for omission of dissipation and pressure work terms are made based on order of magnitude arguments, but thermodynamically speaking, removing these items brings a paradox to entropy generation budget. It should be noted that the momentum equations captures dissipation of momentum due to fluid friction (diffusion terms) but the equivalent dissipated heat is not captured in the energy equation under the OB approximation. In addition, absence of the pressure work in the energy equation causes a mismatch between the internal energy and work done upon the fluid. Using Gibbs and local entropy balance equations, it can be shown that when these terms are neglected in the energy equation, the thermodynamic system described under the OB approximation recognizes only heat conduction as a source of irreversibility and neglects irreversibilities due to viscous friction. This inspired development of a more comprehensive form of the

energy equation under the OB approximation referred to various names such as 'deep convection' [33], 'thermodynamic' [34], and 'extended' [35] Boussinesq approximations. Pons & Le Quéré [36] applied the thermodynamic Boussinesq approximations for natural convection problems and concluded that when the dimensionless adiabatic temperature gradient is larger than 0.01, the pressure work effects are no longer negligible.

In the limit of small temperature differences of the OB operating regime, thermophysical properties of the working fluid are considered as constant. This is a correct assumption as small temperature differences do not impose significant effects on the thermophysical properties of the fluid, but as soon as temperature differences become large enough, the assumption of constant properties may not be valid anymore, especially for working fluids sensitive to temperature differences. The idea of the variable properties (often as a function of temperature) is considered as a separate class of approaches beyond the OB approximation, though in this subcategory, still other fundamentals of the OB approximation are applied. According to Leal *et al.* [37], the property variation effects are considerable even well within the OB regime. Many works have been done in this type of incompressible treatment of the governing equations beyond the OB approximation that are focused on checking/comparing the thermo-flow field when thermophysical properties are considered as constant (OB approximation) or treated variable as a function of temperature or even pressure. This strategy was used by Souza *et al.* [38] where all properties of the working fluid including viscosity, thermal conductivity and also heat capacity were considered as functions of temperature for numerical simulation of NC in an inclined square cavity (including zero leaning angle).

In this article, a simplified Gay-Lussac (SGL) approach is presented for buoyancy driven flows in which density variations are extended to the advection/convection terms of the momentum and energy equations, respectively. In other words, under the SGL approach, density variations are omitted only from the continuity equation. An square cavity benchmark problem is selected to show that the results of the GL and SGL approaches are consistent in both transient and steady state levels, but the SGL has a simpler form with cheaper computational cost. Subsequently, performance of the SGL as an efficient representative of the GL family is tested against the OB and weakly compressible approximations at high relative temperature differences in square cavity benchmark problem with different leaning angles.

The rest of the article is organized as follows: Section 2 presents the aforementioned GL and SGL formulation and also governing equations under the LMS approximation. Section 3 introduces the geometry and boundary conditions of the problem and concerns about numerical considerations including used code accuracy and mesh size dependency. In Section 4, similar performance of the GL and SGL approximations with a reduced computational cost for the SGL approach is proved. In Section 5, the mismatch among SGL, OB and LMS approximations is scrutinized, and finally conclusions are drawn in Section 6.

2. Gay-Lussac and simplified Gay-Lussac approximations

Under the OB approximation, density variations are ignored except within the gravity term. An incompressible non-OB treatment of the governing equation is the GL approach that is established based on considering the density variations beyond the gravity term. Starting with the dimensional form of the incompressible Navier—Stokes equations with thermal transport in the absence of any additional force and negligible viscus heat dissipation,

$$\begin{cases} (\rho/\rho_0)\nabla \cdot u = 0, \\ \partial \boldsymbol{u}/\partial t^* + (\rho/\rho_0)(\boldsymbol{u}\cdot\nabla)u = -(1/\rho_0)\nabla p + \nu\nabla^2\boldsymbol{u} + (\rho/\rho_0)\boldsymbol{e_g}, \\ \partial T/\partial t^* + (\rho/\rho_0)(\boldsymbol{u}\cdot\nabla)T = \alpha\nabla^2 T. \end{cases} \tag{1}$$

Following the OB approach, substitution a linear density state relation ($\rho/\rho_0 = 1 - \beta\theta$) into the governing equation yields

$$\begin{cases} (1-\beta\theta)\nabla\cdot u = 0, \\ \partial \boldsymbol{u}/\partial t^* + (1-\beta\theta)(\boldsymbol{u}\cdot\nabla)u = -(1/\rho_0)\nabla p + \nu\nabla^2\boldsymbol{u} + (\rho/\rho_0)\boldsymbol{e_g}, \\ \partial T/\partial t^* + (1-\beta\theta)(\boldsymbol{u}\cdot\nabla)T = \alpha\nabla^2 T. \end{cases} \tag{2}$$

In Eq. (2), p^* is a modified pressure introduced as $p^* = p + \rho_0\phi$, where ϕ is the gravitational potential. Using dimensionless parameters

$$t = \frac{t^*\alpha}{L^2}, \boldsymbol{X} = \frac{\boldsymbol{x}}{L}, \ \boldsymbol{U} = \frac{\boldsymbol{u}L}{\alpha}, P = \frac{p^*L^2}{\rho\alpha^2}, \ \Theta = \frac{\theta}{\Delta\theta} = \frac{T-T_0}{T_h - T_c}, Ga = \beta\Delta\theta, \tag{3}$$

one can derive the dimensionless form of the governing equation under the GL approximation,

$$\begin{cases} (1-Ga\Theta)\nabla\cdot U = 0, \\ \partial \boldsymbol{U}/\partial t + (1-Ga\Theta)(\boldsymbol{U}\cdot\nabla)U = -\nabla P + Pr\nabla^2\boldsymbol{U} - RaPr\Theta\boldsymbol{e_g}, \\ \partial\Theta/\partial t + (1-Ga\Theta)(\boldsymbol{U}\cdot\nabla)\Theta = \nabla^2\Theta, \\ \Theta(\boldsymbol{X},0) = \boldsymbol{U}(\boldsymbol{X},0) = 0. \end{cases} \tag{4}$$

Eq. (4) introduces the Prandtl number $Pr = \nu/\alpha$ characterizing the ratio of the molecular to thermal dissipation and the Rayleigh number $Ra = g\beta\Delta\theta {L_{\text{ref}}}^3/\nu\alpha$ characterizing the ratio of buoyancy to viscous and thermal dissipation. As seen, governing equations under the OB approximation are recovered as $Ga \to 0$ ($\Delta\theta \to 0$). Under the GL approximation, $(1 - Ga\Theta)$ acts as a modifier on different terms, and its effect becomes more pronounced by increasing Ga (and consequently $\Delta\theta$), but in practice Ga cannot exceed a specified value to avoid an unphysical (negative) density

$$\rho/\rho_0 = 1 - \beta\theta = 1 - \beta\Delta\theta\Theta = 1 - Ga\Theta > 0. \tag{5}$$

Eq. (5) indicates that the maximum Ga cannot exceed 2 ($Ga_{max} = 2$) based on the defined dimensionless temperature. In this study, a simplified Gay-Lussac (SGL) approximation is proposed by omitting density variations only from the continuity equation

$$\begin{cases} \nabla\cdot U = 0, \\ \partial \boldsymbol{U}/\partial t + (1-Ga\Theta)(\boldsymbol{U}\cdot\nabla)U = -\nabla P + Pr\nabla^2\boldsymbol{U} - RaPr\Theta\boldsymbol{e_g}, \\ \partial\Theta/\partial t + (1-Ga\Theta)(\boldsymbol{U}\cdot\nabla)\Theta = \nabla^2\Theta, \\ \Theta(\boldsymbol{X},0) = \boldsymbol{U}(\boldsymbol{X},0) = 0. \end{cases} \tag{6}$$

As seen, the governing equations under the SGL approximation are consistent with the governing equations under the OB approximation, except for the pre-factors of the advection/convection terms in the momentum and energy equations, respectively. The roles of these pre-factors are to modify the strength of the advection/convection terms locally throughout the flow, physics that is ignored in the OB approximation. Indeed, regions of the thermo-flow field having a higher magnitude of the non-OB advection/convection described by $|\Theta(\boldsymbol{U}\cdot\nabla)\boldsymbol{U}|$ and $|\Theta(\boldsymbol{U}\cdot\nabla)\Theta|$, respectively, will experience more deviations from the OB buoyancy approximation. The strength of the pre-factors modification is proportional to Ga, magnitude with $Ga \to 0$ ($\Delta\theta \to 0$) recovering the classical OB approximation. The GL-parameter is a product of Rayleigh, Prandtl, and Froude numbers ($Ga = RaPrFr$) where the Froude number characterizes the ratio of inertia to gravity. Thus, another form of the governing equations under the SGL approximation may be expressed as

$$\begin{cases} \nabla \cdot \boldsymbol{U} = 0, \\ \partial \boldsymbol{U}/\partial t + (1 - RaPrFr\Theta)(\boldsymbol{U} \cdot \nabla)\boldsymbol{U} = -\nabla P + Pr\nabla^2 \boldsymbol{U} - RaPr\Theta \boldsymbol{e_g}, \\ \partial \Theta/\partial t + (1 - RaPrFr\Theta)(\boldsymbol{U} \cdot \nabla)\Theta = \nabla^2 \Theta. \end{cases} \tag{7}$$

As mentioned earlier, in this study results are compared against the LMS approximation. Governing equations under the LMS approximation are expressed as [25–27]

$$\begin{cases} \partial \rho/\partial t^* + \nabla \cdot (\rho \boldsymbol{u}) = 0, \\ \partial(\rho \boldsymbol{u})/\partial t^* + \nabla \cdot (\rho \boldsymbol{u} \otimes \boldsymbol{u}) = -\nabla p^* + \ \nabla \cdot \boldsymbol{\tau} + \rho g \boldsymbol{e}_g, \\ \rho c_p(\partial T/\partial t^* + \boldsymbol{u} \cdot \nabla T) = k\nabla^2 T + \mathrm{d}p_{\mathrm{th}}/\mathrm{d}t^*, \\ P_{th} = \rho RT, \\ T(\boldsymbol{X}, 0) = T_0, p_{th}(0) = p_0, \boldsymbol{u}(\boldsymbol{x}, 0) = 0. \end{cases} \tag{8}$$

In Eq. (8), $p_{\mathrm{th}}(t)$ is the (spatially uniform) thermodynamic pressure, and c_p is the specific heat at constant pressure, which may be expressed in terms of heat capacity ratio ($\eta = c_p/c_v$) and the gas constant (R) as $c_p = \eta R/(\eta - 1)$. Also, $\boldsymbol{\tau}$ is the stress tensor that under Stokes's hypothesis for bulk viscosity ($\lambda = -2/3\mu$) is defined as

$$\boldsymbol{\tau} = \nabla \boldsymbol{u} + (\nabla \boldsymbol{u})^T - 2/3(\nabla \cdot \boldsymbol{u})\boldsymbol{I}. \tag{9}$$

In natural convection simulation via compressible/weakly-compressible approach, Prandtl number is introduced as defined earlier, but the Rayleigh number is expressed slightly differently compared to the incompressible flow, as

$$Ra = 2\varepsilon Pr \frac{g{\rho_0}^2 L^3}{{\mu_0}^2}. \tag{10}$$

In Eq. (10), ε is the relative temperature difference defined as $\varepsilon = (T_h - T_c)/2T_0$, so that $T_h = T_0(1 + \varepsilon)$ and $T_c = T_0(1 - \varepsilon)$. Comparing ε and Ga definitions gives an interesting relation for the Froude number at each Rayleigh and Prandtl number, as

$$\underbrace{2\varepsilon = (T_{\mathrm{h}} - T_{\mathrm{c}})/T_o}_{\text{Compressible}} = \underbrace{\beta \Delta\theta = Ga = RaPrFr}_{\text{Incompressible}} \rightarrow Fr = 2\varepsilon/RaPr. \tag{11}$$

Another advantage of Eq. (11) is expressing Ga by the relative temperature difference definition ($Ga = 2\varepsilon$). Thus, another form of the governing equations under the SGL approximation may be obtained using ε instead of Ga and/or three dominant dimensionless parameters i.e. Ra, Pr and Fr as

$$\begin{cases} \nabla \cdot \boldsymbol{U} = 0, \\ \partial \boldsymbol{U}/\partial t + (1 - 2\varepsilon\Theta)(\boldsymbol{U} \cdot \nabla)\boldsymbol{U} = -\nabla P + Pr\nabla^2 \boldsymbol{U} - RaPr\Theta \boldsymbol{e_g}, \\ \partial \Theta/\partial t + (1 - 2\varepsilon\Theta)(\boldsymbol{U} \cdot \nabla)\Theta = \nabla^2 \Theta \end{cases} \tag{12}$$

Finally, it should be noted that the physical range of the relative temperature difference ($0 \leq \varepsilon \leq 1$), gives a consistent constraint for physical range of Ga ($0 \leq Ga \leq 2$).

3. Description of the problem and numerical method

A schematic of the considered problem, i.e. square cavity at an inclination angle of γ which is considered equal to 0 and $\pm\pi/6$ in this study, is depicted in Figure 1. The applied thermal boundary conditions include two constant temperature and two adiabatic walls with a zero velocity boundary condition along all surfaces. For this problem, the reference length is equal to one

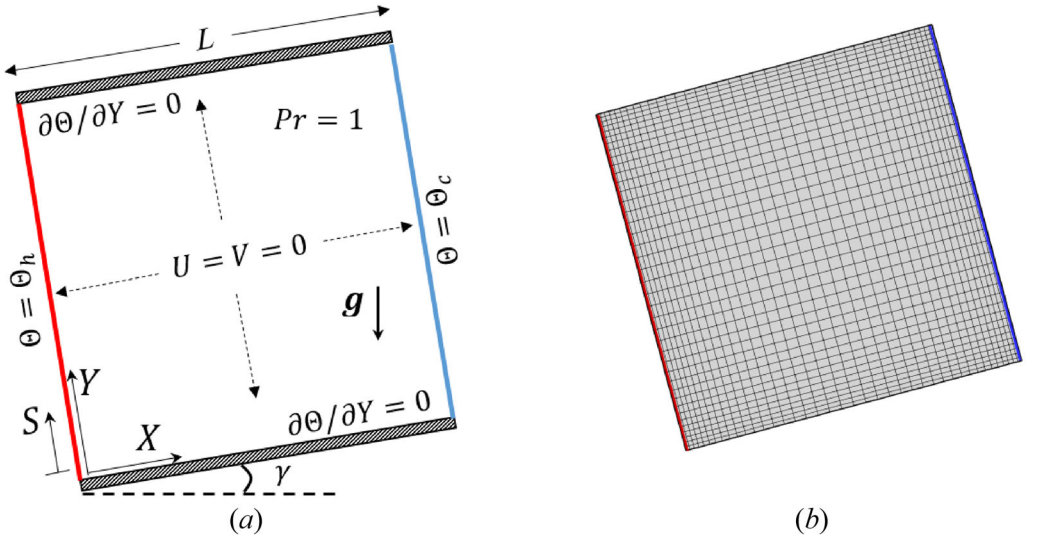

Figure 1. A schematic representation of the problem including (*a*) applied boundary conditions and (*b*) a coarse computational grid having 40 × 40 quadrilateral elements depicted at a positive leaning angle.

side length of the geometry ($L_{ref} = L$). The physical domain is meshed using quadrilateral elements. A schematic coarse mesh is shown for illustration purposes in Figure 1.

The local and average Nusselt number along the two constant-temperature surfaces are calculated from

$$Nu_{\text{loc}}(S) = -\left.\frac{\partial \Theta}{\partial \boldsymbol{n}}\right|_{\text{wall}}, \tag{13}$$

$$Nu_{\text{avg}} = \int_0^1 Nu_{\text{loc}}\ \mathrm{d}S. \tag{14}$$

In Eq. (13), $\boldsymbol{n}$ is the unit outward normal vector to the surface. The friction coefficient along the internal surfaces is calculated from

$$\boldsymbol{c_f} = -2Pr\begin{bmatrix}\tau_{xx} & \tau_{xy}\\ \tau_{yx} & \tau_{yy}\end{bmatrix}\begin{bmatrix}n_x\\ n_y\end{bmatrix} = -2Pr\begin{bmatrix}2\partial U/\partial X & \partial U/\partial Y + \partial V/\partial X\\ \partial U/\partial Y + \partial V/\partial X & 2\partial V/\partial Y\end{bmatrix}\begin{bmatrix}n_x\\ n_y\end{bmatrix}, \tag{15}$$

where n_x and n_y are the horizontal and vertical components of the wall-normal vector, respectively. The friction coefficient magnitude is defined as

$$c_f = \sqrt{(c_{f_x})^2 + (c_{f_y})^2} \tag{16}$$

where,

$$c_{f_x} = -2Pr\left[(2\partial U/\partial X)n_x + (\partial U/\partial Y + \partial V/\partial X)n_y\right], \tag{17}$$

$$c_{f_y} = -2Pr\left[(\partial U/\partial Y + \partial V/\partial X)n_x + (2\partial V/\partial Y)n_y\right]. \tag{18}$$

The governing equations are solved using a control volume finite-element method (CVFEM) solver employing a fractional step method with second order temporal accuracy (Adams Bashforth/Crank—Nicolson) for the time dependent equations. The nonlinear advection/convection terms are Discretized using both 2$^{\text{nd}}$-order upwind and central schemes, while diffusion terms are Discretized via central schemes. In CVFEM, a unique control volume (as shown in

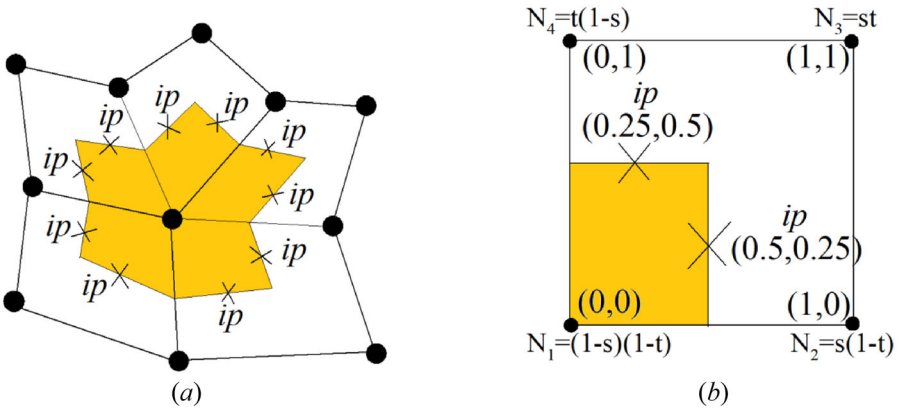

Figure 2. A schematic of unstructured quadrilateral elements: (*a*) a typical control volume associated with integration points (*b*) local coordinate (*s,t*) and bilinear shape functions in a standard element.

Figure 2(*a*)) is assigned to each node. The boundaries of each control volume are comprised of a number of planar panels and an integration point (*ip*) is assigned at the middle of each panel. Integration of the diffusion term over the control volume and applying the Gauss divergence theorem yields

$$\int_{v_p} \nabla^2 \boldsymbol{U} \mathrm{d}v = \oint_{A_p} \nabla \boldsymbol{U}_{ip} \cdot \mathrm{d}\boldsymbol{A} = \sum_{ip=1}^{n} \nabla \boldsymbol{U}_{ip} \cdot \boldsymbol{A}_{\boldsymbol{ip}}. \tag{19}$$

In Eq. (19), n is the number of integration points surrounding the main node and $\boldsymbol{A}_{\boldsymbol{ip}}$ is the normal vector surface at each *ip*. Using bilinear shape functions ($N_j(s,t)$), any parameter (such as $\boldsymbol{U}$) within the element with a local coordinate (s,t) is related to the nodal values via weighted values provided by shape functions

$$\boldsymbol{U}_{ip} = \boldsymbol{U}(s,t) = \sum_{j=1}^{4} N_j(s,t) \boldsymbol{U}_j. \tag{20}$$

The shape functions relating *ip* values to the nodal values for a quadrilateral element are shown in Figure 2(*b*). The diffusion operator may be expressed as follows

$$\mathrm{D}(\boldsymbol{U}) = \sum_{ip=1}^{n} \sum_{j=1}^{4} \omega_j \nabla N_j \cdot \boldsymbol{A}_{\boldsymbol{ip}}. \tag{21}$$

Since the bilinear shape functions are functions of their local coordinate system, their gradients with respect to the global coordinate system are calculated using the chain rule. In Eq. (21), the effect of all nodes surrounding an *ip* (such as the one shown in Figure 2(*b*)) are considered by weighted values. The diffusion operator in the energy equation is calculated in a similar fashion.

In the governing equations, nonlinear convection/advection terms are linearized using lagged values from the previous iteration. For instance, integration of the advection term over the control volume and applying Gauss divergence theorem yields

$$\int_{v_p} \boldsymbol{U} \cdot \nabla \overline{\boldsymbol{U}} \mathrm{d}v = \oint_{A_p} \boldsymbol{U}\left(\overline{\boldsymbol{U}} \cdot \boldsymbol{A}_{\boldsymbol{ip}.}\right) = \sum_{ip=1}^{n} \boldsymbol{U}_{ip}\left(\overline{\boldsymbol{U}}_{\boldsymbol{ip}} \cdot \boldsymbol{A}_{\boldsymbol{ip}.}\right). \tag{22}$$

Using bilinear shape functions (Eq. (20)) to relate the integral point values to the nodal values yields

Table 1. Comparison of the present calculated local and average Nusselt number by CVFEM solver (bold) with published benchmarks.

	Quantity	Present study	Davis [3]	Wan *et al.* [7]	Ashrafizadeh & Nikfar [8]
$Ra = 10^4$	Nu_{max} (at Y)	**3.548 (0.140)**	3.53 (0.143)	3.597 (0.13)	3.531 (0.139)
	Nu_{min} (at Y)	**0.589 (1.0)**	0.586 (1.0)	0.577 (1.0)	0.584 (1.0)
	Nu_{avg}	**2.23**	2.42	2.25	2.24
$Ra = 10^5$	Nu_{max} (at Y)	**7.778 (0.075)**	7.71 (0.08)	7.945 (0.08)	7.720 (0.084)
	Nu_{min} (at Y)	**0.734 (1.0)**	0.729 (1.0)	0.698 (1.0)	0.726 (1.0)
	Nu_{avg}	**4.51**	4.52	4.60	4.52
$Ra = 10^6$	Nu_{max} (at Y)	**17.633 (0.038)**	17.92 (0.038)	17.86 (0.03)	17.732 (0.039)
	Nu_{min} (at Y)	**0.996 (1.0)**	0.989 (1.0)	0.913 (1.0)	0.975 (1.0)
	Nu_{avg}	**8.82**	8.92	8.98	8.83
$Ra = 10^7$	Nu_{max} (at Y)	**40.253 (0.015)**	N. A.	38.60 (0.015)	39.457 (0.015)
	Nu_{min} (at Y)	**1.286 (1.00)**	N. A.	1.298 (1.00)	1.315 (1.00)
	Nu_{avg}	**16.51**	N. A.	16.66	16.54

$$N(\boldsymbol{U}) = \sum_{ip=1}^{n} \sum_{j=1}^{4} \boldsymbol{U}_j N_j \left(\overline{\boldsymbol{U}}_{\boldsymbol{ip}} \cdot \boldsymbol{A}_{\boldsymbol{ip}_\cdot} \right). \tag{23}$$

Similarly, in Eq. (23) n is the number of ip surrounding the main node. If the lagged values in Eq. (23) (which are denoted by an overbar) disrespected of the flow direction to be approximated from nodal values within the element via weighted values from the, then the approximation is equivalent to the central scheme. Another possible Discretization is approximating lagged values considering flow direction, which is known as the upwind scheme. The nonlinear convection term in the energy equation is calculated in a similar fashion. Iterative solution procedure is stopped as soon as the maximum difference of variables during two successive iterations becomes less than 10^{-7}. Accurate performance of the used solver is already tested [39–47] but here it is further validated against refs. [3, 7, 8] in terms of the local and average Nusselt number of square cavity with zero inclination angle at four different Rayleigh number, adopting air as the working fluid ($Pr = 0.71$) in Table 1. A close agreement is observed.

Accurate performance of the CVFEM solver under the LMS approximation is also validated against ref. [48] in terms of the average Nusselt number and thermodynamic pressure at two Rayleigh numbers $Ra = 10^6$ and 10^7 at $\varepsilon = 0.6$ with air as the working fluid ($Pr = 0.71$) in two states including constant and variable properties (see Table 2). The present simulations recover published values very well, with discrepancies lower than 1.97%.

Mesh dependence is checked for the CVFEM solver in Table 3 at $Ra = 10^7$ and $Pr = 1$ under the OB approximation ($Ga = 0$) and under the GL approach at the highest Ga value in this study ($Ga = 0.6$). Results indicate that 124 nodes in each direction is enough for mesh independence for both incompressible approximations.

Mesh dependence of the CVFEM solver under the LMS approximation is also checked in Table 4 at the highest Rayleigh number $Ra = 10^7$ and $Pr = 1$ for the highest relative temperature difference ($\varepsilon = 0.3$) in this study. It is found using 124 nodes ($n_x \times n_y = 124^2$) in each direction guarantees results independence from the mesh size for the weakly compressible approach. Similar dependence is also found for the inclined cavity cases but for the sake of brevity, they are not mentioned here.

4. Comparing results under the GL and SGL approaches and computational cost

In this section, results obtained under the GL and SGL approaches are compared. In other words, it is shown the GL and SGL approaches give similar results in both transient and steady states. The mismatch in steady state solutions under the two approaches is investigated by calculation of the absolute difference in temperature and velocity magnitude in the square cavity with $\gamma = 0$ at

Table 2. Comparison of the present calculated local and average Nusselt number by CVFEM solver (bold) with published benchmarks.

	Quantity	Present study	Le Quéré *et al.* [48]	|difference|%
$Ra = 10^6,\ \varepsilon = 0.6$	P_{th}	0.858	0.856	0.23
Constant properties	Nu_{ave}	8.895	8.859	0.40
$Ra = 10^6,\ \varepsilon = 0.6$	P_{th}	0.921	0.924	0.32
Variable properties	Nu_{ave}	8.693	8.686	0.08
$Ra = 10^7,\ \varepsilon = 0.6$	P_{th}	0.920	0.922	0.21
Variable properties	Nu_{ave}	16.461	16.241	1.33

$Ra = 10^7,\ Pr = 1$ and $Ga = 0.6$ $(\varepsilon = 0.3)$. The results are shown in Figures 3(*a*) and (*b*), respectively. The maximum absolute temperature and velocity magnitude differences in Figures 3(*a*) and (*b*) are approximately 0.0025 and 2.5, respectively, which ranges within 0.5% and 0.35% of the temperature and velocity magnitude values. Interestingly, the largest differences in velocity magnitude occur at top-left and bottom-right regions of the cavity. These regions correspond to where flow traveling adjacent to the hot and cold boundaries deflects horizontally. The longitudinal transport along the top and bottom walls is then perturbed, resulting in the largest temperature difference being detected in those regions.

Similar output/behavior of the GL and SGL approximations in the transient state is investigated in Figure 4 in the context of the absolute local Nusselt number and friction coefficient differences along the vertical surfaces of the square cavity with $\gamma = 0$ at $Ra = 10^7,\ Pr = 1$ and $Ga = 0.6$. Results indicate the absolute local Nusselt number difference is three orders smaller than the local Nusselt number magnitude during transient solution $(O(|\Delta Nu_{loc}|/Nu_{loc}) \sim 0.001)$. A similar comparison for the absolute local friction coefficient difference shows a value of five order smaller value, i.e. $O\left(|\Delta c_f|/c_f\right) \sim 10^{-5}$.

Computational cost and convergence histories of the GL and SGL approaches are also investigated in Figures 5(*a*) and (*b*), respectively. To compare computational cost, CPU-time is calculated at $Ra = 10^7,\ Pr = 1$ and $Ga = 0.6$ in two states in which advection/convection terms are Discretized using upwind or central schemes. Bar charts of Figure 5(*a*) shows a 17% and 11% lower computational cost for the SGL compared to the GL approximation for the central and upwind schemes, respectively. Convergence rates of the two approaches are also checked in terms of the velocity components and temperature tolerance in Figure 5(*b*). The tolerance of any scalar in this study is defined as the maximum alteration of all nodal values during two successive iterations. Results in Figure 5(*b*) indicate that both approaches have similar convergence rate and omitting density variations from the continuity equation merely simplifies the formulation and reduces the computational cost. Having demonstrated that the GL and SGL approximations exhibit identical behavior, we consider only the SGL approximation hereafter.

5. Results under the SGL, OB, and LMS approximations

In this section, results under the SGL, OB and LMS approximations are compared. Simulations are performed at $Pr = 1$ up to $Ra = 10^7$ $(10^2 \leq Ra \leq 10^7)$ and $\varepsilon = 0.3$ $(0 \leq \varepsilon \leq 0.3)$. It should be noted that a relative temperature difference of 0.01 is considered as a differential relative temperature difference and is representative of a OB case. Here, we extend this parameter to 30 times larger, beyond the validity of the OB approximation. Studying relative temperature differences exceeding 0.3 is beyond the scope and goals of this article. The considered range for ε gives $0 \leq Ga \leq 0.6$. For the considered range of the pertinent parameters, it is supposed that the flow field is 2 D, laminar and stable.

For a better understanding of the thermo-flow fields produced under the different approximations, absolute temperature differences of the weakly compressible approach at $Ra = 10^7$ and

Table 3. Mesh resolution study for average Nusselt number at $Ra = 10^7$ and $Pr = 1$.

	$n_x \times n_y$	31^2	62^2	124^2	248^2
OB approximation	Nu_{ave}	13.281114	13.812208	13.932074	13.932074
($Ga = 0$)	|difference|	–	0.531094	0.119866	0.000000
SGL approximation	Nu_{ave}	13.245957	13.772384	13.890921	13.890921
($Ga = 0.6$)	|difference|	–	0.526427	0.118537	0.000000

Table 4. Mesh resolution study for average Nusselt number and thermodynamic pressure at $Ra = 10^7$, $Pr = 1$, and $\varepsilon = 0.3$.

	$n_x \times n_y$	62^2	124^2	248^2
LMS approximation	P_{th}	0.9601	0.9677	0.9677
	|difference|	–	0.0076	0.000000
	Nu_{ave}	13.9613	14.0476	14.0476
	|difference|	–	0.0863	0.000000

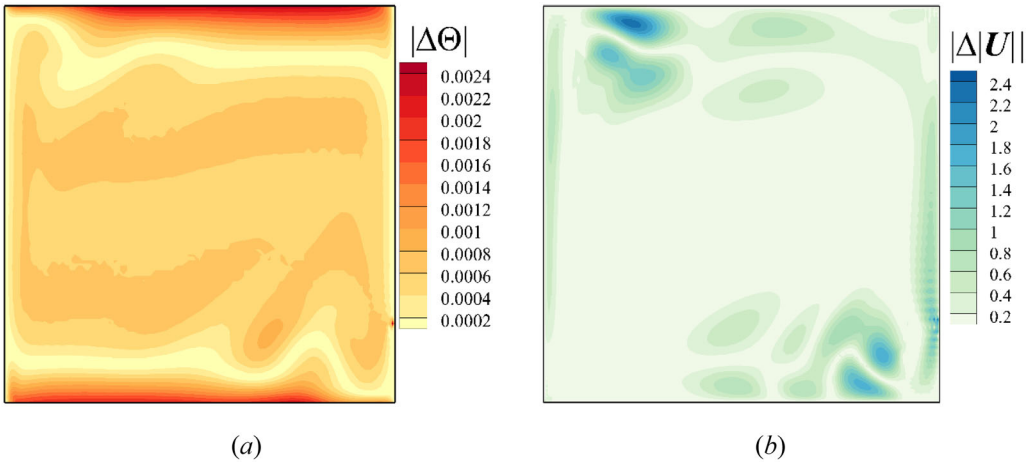

Figure 3. Comparing results under the GL and SGL approximations at $Ra = 10^7$, $Pr = 1$, and $Ga = 0.6$ for (*a*) absolute temperature difference and (*b*) absolute velocity magnitude difference.

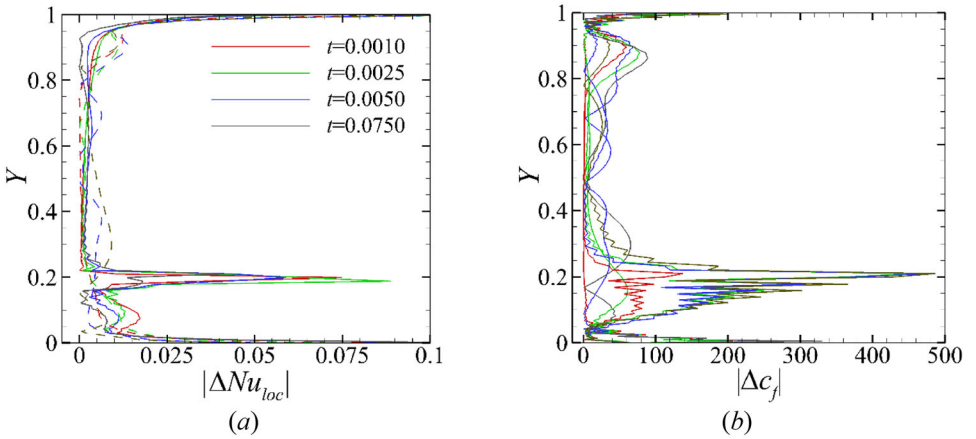

Figure 4. Comparing transient local Nusselt number and coefficient friction differences along the vertical walls of the square cavity with $\gamma = 0$ under the GL and SGL approximations at $Ra = 10^7$, $Pr = 1$, and $Ga = 0.6$: (*a*) absolute local Nusselt number differences and (*b*) absolute local coefficient friction differences. In both figures, solid lines represent data of the left (hot) wall while dashed lines represent data of the right (cold) wall.

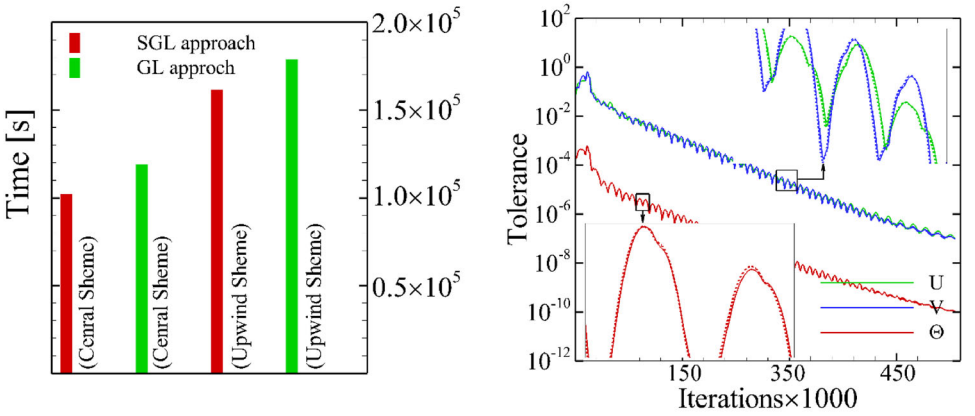

Figure 5. Comparing convergence rate and computational cost of the GL and SGL approximations at $Ra = 10^7$, $Pr = 1$, and $Ga = 0.6$: (*a*) elapsed time under the two approaches using central and upwind schemes and (*b*) convergence history. In convergence history plot, solid lines represent the GL approach while dashed lines show the SGL approach.

$\varepsilon = 0.3$ ($Ga = 0.6$) against the OB and SGL approximations are depicted in Figures 6(*a–f*). Absolute temperature differences under the different approaches shift isotherms, with larger differences found for the zero inclination angle cavity compared to the negative and positive inclination angles. In the zero inclination angle case (Figures 6(*b*) and (*e*)), the difference is largest at the top-left and bottom-right corners, while in the positive inclination angle case (Figures 6(*c*) and (f)) it is occurring almost evenly over the interior region with a focus along the two adiabatic sides. For the negative inclination angle case (Figures 6(*a*) and (*d*)), larger differences occur along the isothermal wall. Regions with smaller temperature differences may be attributed to different situations of the fluid decelerated with respect to the geometry. For instance, negligible differences of the temperature fields in the negative inclination angle case across the top-left corer may be attributed to the enforced downward flow direction by the geometry that is in conflict with the upward buoyancy-driven flow at that region. The maximum absolute temperature difference in the square cavity with $\gamma = 0$ is approximately 12% of the temperature range within the enclosure (with a slightly larger difference for the SGL approximation), reflecting a mismatch of this magnitude between the weakly compressible and incompressible approaches. A similar comparison for the negative/positive inclination angle cases shows a smaller difference approximately 5% mismatch between the compressible and incompressible approximations. The SGL approach shows a better performance in the negative inclination angle case compared to the OB approximation in the interior while both approaches show a similar deviation from the LMS approximation in the positive inclination angle case. It is expected that the mismatch between the aforementioned approaches to be augmented by increasing the relative temperature difference.

To appreciate the role of non-Boussinesq term effects in the advection/convection terms of the governing equation under the SGL approximation, the magnitude of $|\Theta((\boldsymbol{U}\cdot\nabla)\boldsymbol{U})|$ and $|\Theta((\boldsymbol{U}\cdot\nabla)\Theta)|$ under the OB approximation is portrayed for the square cavity with different inclination angels at $Ra = 10^7$ in Figures 7(*a–f*). As seen, the magnitude of the non-Boussinesq term in the momentum equation is stronger along the isothermal walls and especially at the four corners of the cavity, though weaker effects are found within the central regions of the enclosure. Stronger non-Boussinesq effects in the momentum equation along the isothermal walls may be attributed to larger velocity gradients since fluid adjacent to the wall is accelerated by buoyancy force as it reaches to the wall during circulation and decelerated as it gets close to the end of the path parallel to the isotherm wall. Stronger non-Boussinesq effects in the momentum equation at the four corners is attributed to fluid rotation to adjust its motion with respect to the geometry

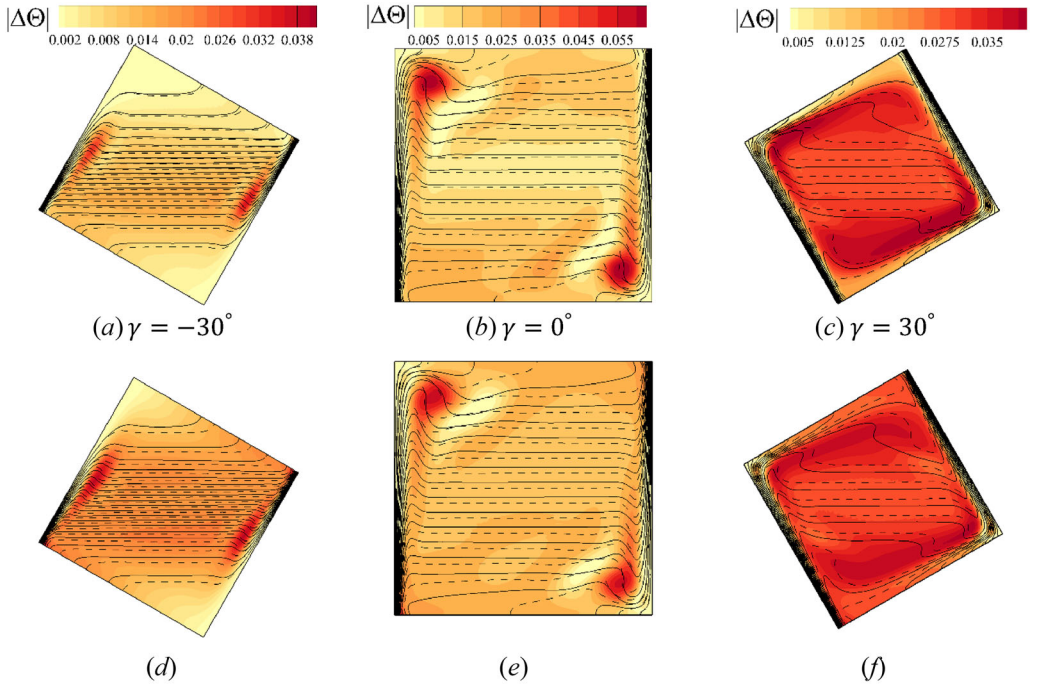

Figure 6. Results at $Ra = 10^7$, $Pr = 1$, and $\varepsilon = 0.3$ (*a, b, c*): absolute temperature difference between the SGL and LMS approximations (*d, e, f*) and absolute temperature difference between the OB and LMS approximations. Solid lines represent the LMS approximation isotherms, while dashed lines show the compared approach.

corners. It is found that the non-Boussinesq term magnitude in the momentum equation is smaller for the negative inclination angel cavity compared to the zero and positive inclinations cases. The magnitude of the non-Boussinesq term in the energy equation has a similar pattern, as it is stronger along the isothermal walls and especially at top-right and bottom-left corners. Stronger non-Boussinesq effects in the energy equation in these regions may be attributed to the larger temperature gradients. This is clear from Figure 6, where isotherm lines are accumulated across the top-right and bottom-left corners that result in larger temperature gradients across those regions. Results also indicate that, the magnitude of the non-Boussinesq term in the momentum equation ($|\Theta((\boldsymbol{U}\cdot\nabla)\boldsymbol{U})|$) is larger than the non-Boussinesq term in the energy equation ($|\Theta((\boldsymbol{U}\cdot\nabla)\Theta)|$), though, a fair comparison should be made based on the magnitude of the mentioned terms in their equations. For the square cavity with zero inclination angle at $Ra = 10^7$, the maximum dimensionless velocity magnitude obtained is approximately 715. Comparing the maximum magnitude of $|\Theta((\boldsymbol{U}\cdot\nabla)\boldsymbol{U})|$ (that is portrayed in Figure 7(*b*)) to the maximum dimensionless velocity magnitude gives a value of approximately 840. Similarly, dividing the maximum value of $|\Theta((\boldsymbol{U}\cdot\nabla)\Theta)|$ in the energy equation (that is portrayed in Figure 7(*e*)) to the maximum dimensionless temperature yields a value of approximately 480, concluding that under the Gay-Lussac approach, velocity is more affected by the corresponding non-Boussinesq term rather than temperature field. In this respect, vorticity absolute differences under the three approximations at $Ra = 10^7$ and $\varepsilon = 0.3$ are portrayed for the square cavity with different inclination angles in Figure 8. Comparing obtained results from different approaches reveals that when the buoyancy driven flow is simulated via the weakly compressible approach for large relative temperature difference, the same pattern of vorticity field is formed and the difference mainly comes from vortices (with different strengths) stretching or location shifting through the flow field. In these figures, large values of the vorticity absolute differences are primarily elongated adjacent to the isotherm walls where flow accelerates due to buoyancy force. Finally, vorticity

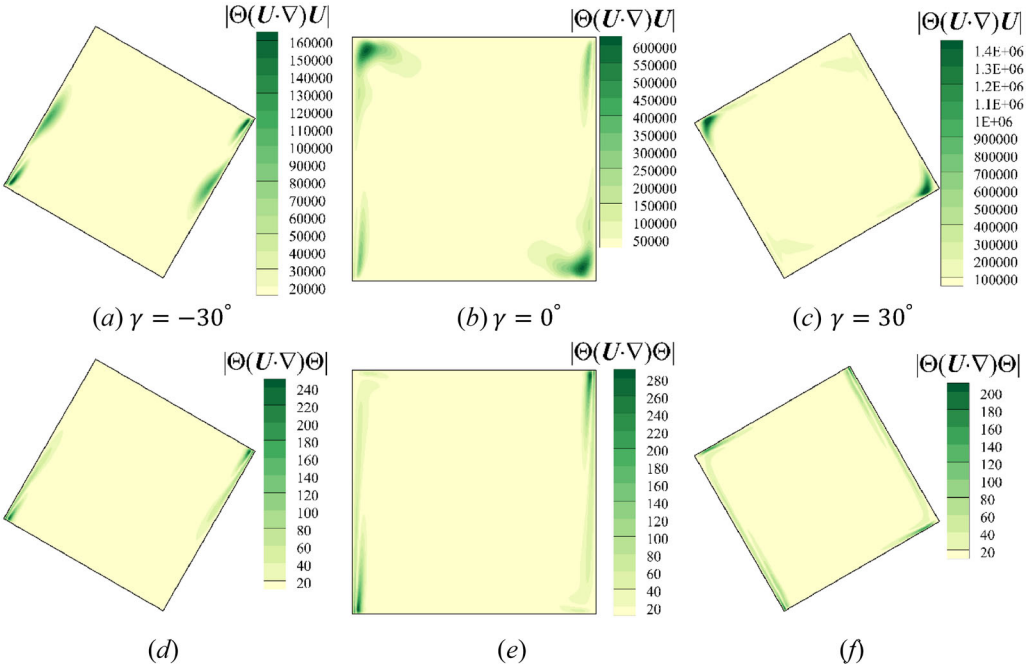

Figure 7. Magnitude of the non-OB advection/convection terms obtained from simulation under the OB approximation for square cavity with different inclination angle (*a, d*) $\gamma = -30^{\circ}$, (*b, e*) $\gamma = 0^{\circ}$, and (*c, f*) $\gamma = 30^{\circ}$.

differences results of different approaches indicate even larger non-Boussinesq term that results in significant modifications in the momentum equation does not create a considerable superior results for the SGL approach compared to the OB approximation.

5.1. Local Nusselt number

The local Nusselt number distribution along the isothermal walls under the different approximations are plotted in Figure 9 at $Ra = 10^7$, $Pr = 1$ and $\varepsilon = 0.3$ for square geometry with the different leaning angles. As seen, the local Nusselt number distributions versus surface length is reversed between the two isothermal walls for all cases. This may be attributed to the increasing and decreasing thermal boundary layer thickness along the isothermal walls in flow direction for the hot and cold walls, respectively. For the square cavity with zero and negative inclination angles (Figures 9(*a*) and (*b*)), there is a monotonic distribution of the local Nusselt number with a local optimum at the bottom-left and top-right corners, but for the positive inclination angle case (Figures 9(*c*)) this changes to an oscillating behavior having smaller local Nusselt number value resembling the Rayleigh–Bénard configuration. Comparing the local Nusselt number distributions along the isothermal walls for the zero and negative inclination angles cases show a clear mismatch between the incompressible and compressible approximations across the bottom-left and top-right corners while the difference is visible along almost all of the two isothermal surfaces for the positive inclination angle case. Results indicate that the SGL approach has a better performance across the bottom-left corner while the OB approximation gives more accurate results across the top-right region.

5.2. Average Nusselt number

The variations of the average Nusselt number across $10^2 \leq Ra \leq 10^7$ is studied at $\varepsilon = 0.15$ and 0.3 under different approximations in Figure 10. Average Nusselt number under the LMS

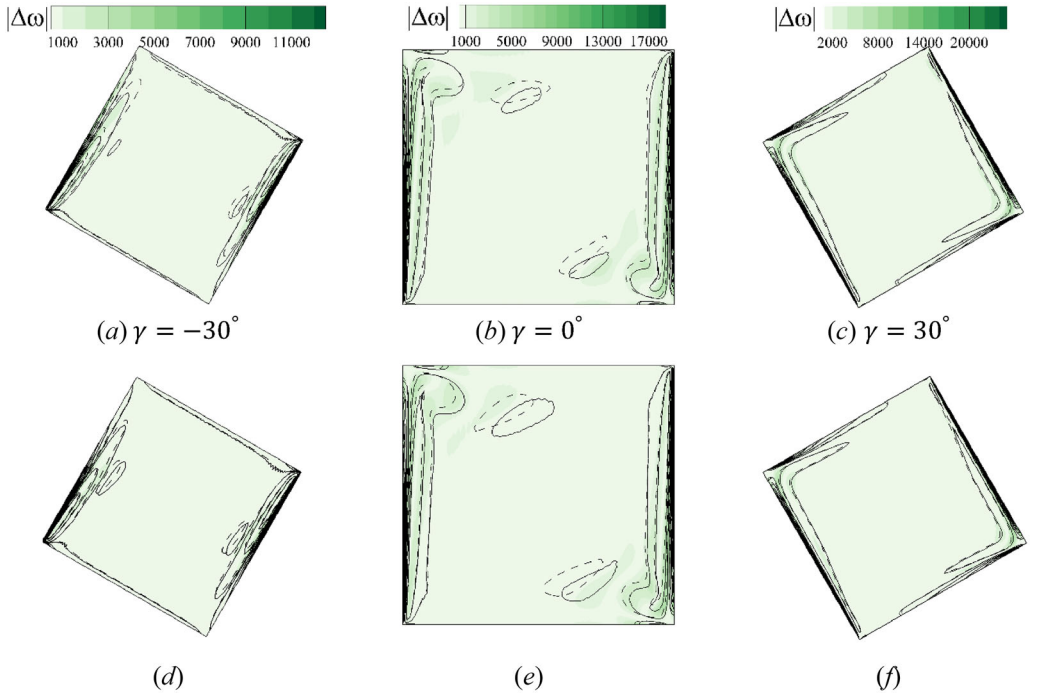

Figure 8. Absolute vorticity differences at $Ra = 10^7$, $Pr = 1$, and $\varepsilon = 0.3$: (*a-c*) SGL and LMS approximations (*d-f*) OB and LMS approximations. In all figures, solid lines represent vorticity under the LMS approximation while dashed lines show vorticity under the other approach. Minimum and maximum of contour levels are equal in each column.

approximation for different inclination angles is plotted at $\varepsilon = 0.15$ and 0.3 in Figures 10(*a*) and (*b*), respectively. As expected, the average Nusselt number increases with increasing Rayleigh number. Since the values of the average Nusselt number under the different approximations are similar, the absolute average Nusselt number differences between the LMS and the two considered incompressible approximations are plotted in separate frames in Figures 10(*c–f*). Due to negligible difference of the average Nusselt number between the OB and SGL approximations that comes from the close results of their local Nusselt number distributions, their difference are not shown here. Comparing the average Nusselt number slope versus the Rayleigh number in Figures 10(*a*) and (*b*) reveals that negative inclination angle decreases the total heat transfer rate. It is also found that a zero inclination angle square cavity has a larger average Nusselt number compared to the both positive and negative inclination angles.

For the average Nusselt number, some of the difference between the compressible and incompressible approximations are nullified by opposite behavior of the local Nusselt number distributions. For instance, in the square cavity with zero inclination angle (Figures 9(*a*) and (*b*)), the approximation that has a lower local Nusselt number distribution along $0 \leq S \leq 0.5$ has a larger value at $0.5 \leq S \leq 1$ and vice versa. This diminishes the difference of the local Nusselt number distribution and gives a smaller difference of the average Nusselt number for the compressible and incompressible approaches. However, the total differences of the average Nusselt number for both incompressible approximations increases by increasing the Rayleigh number, but it does not exceed 2 in the considered range of γ, ε and Ra in this study. Besides, by increasing the relative temperature difference, the difference of the average Nusselt number is increased. Results indicate both positive and negative inclination angles show a considerable average Nusselt number difference in the range of $Ra \geq 10^4$ with an almost linear growth rate while for the zero inclination angle case, the difference grows rapidly in the range of $Ra \geq 10^5$.

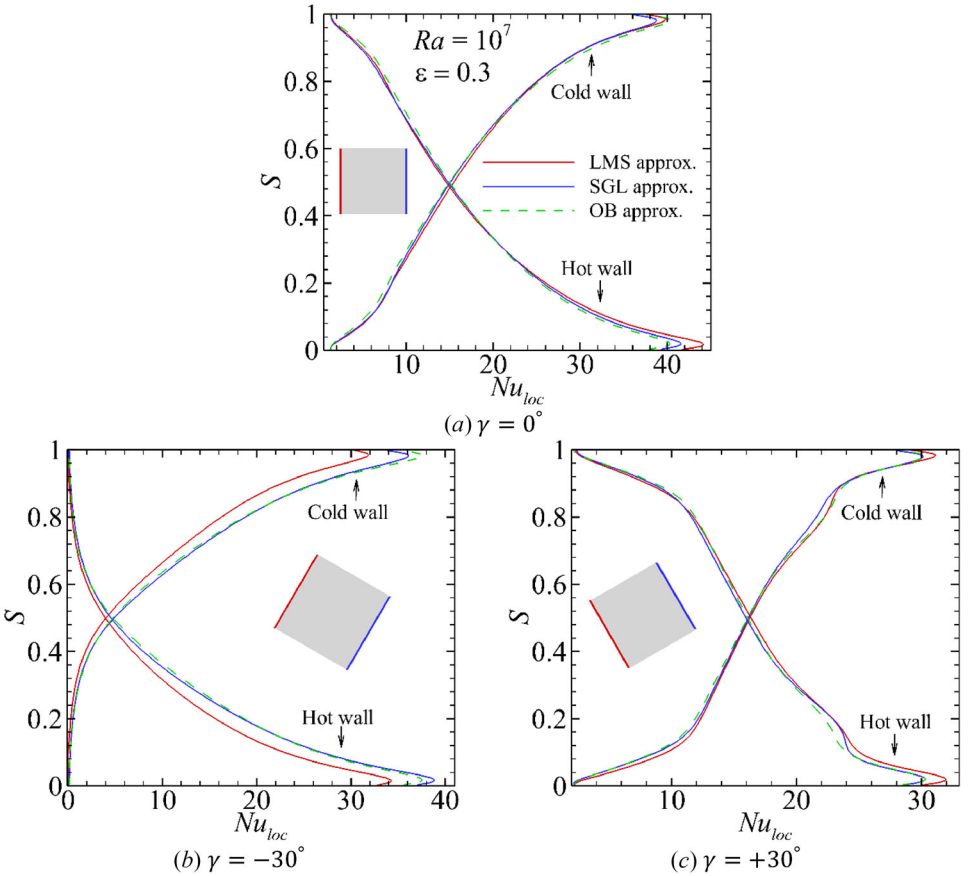

Figure 9. Local Nusselt number distribution along the isothermal walls at $Ra = 10^7$, $Pr = 1$, and $\varepsilon = 0.3$ in square with different inclination angles (*a*) $\gamma = 0°$, (*b*) $\gamma = -30°$, and (*c*) $\gamma = +30°$.

5.3. Skin friction

Local friction coefficient along the isothermal walls is investigated at $Ra = 10^7$, $\varepsilon = 0.15$ and $\varepsilon = 0.3$ under the different approximations in Figure 11. Results show a considerable mismatch between the weakly compressible and incompressible approximations. A comparison among c_f results at $\varepsilon = 0.15$ (Figures 11(*a*), (*c*) and (*e*)) and $\varepsilon = 0.3$ (Figures 11(*b*), (*d*) and (*f*)) reveals that this discrepancy increases with an increase in the relative temperature differences. Indeed, by increasing the relative temperature difference, incompressible approximations show more deviations from the compressible approach. Presented results in Figure 11 indicate that extending the density variations to the advection/convection terms via the linear density state equation does not impose a significant impact on the local friction coefficient as c_f results of the incompressible approximations are attached together in most of the regions.

For the zero inclination angle (Figure 11(*a*)) at $\varepsilon = 0.15$, results of the local coefficient friction indicate that the SGL approach works slightly better than the OB approximation along the hot wall. By increasing the relative temperature difference to 0.3, c_f along the hot wall under the SGL approach deviates from the LMS approximation, especially over $0.55 \leq S \leq 0.85$, but it achieves a better performance than the OB approximation at $0.45 \leq S \leq 0.55$. For the cold wall, by increasing the relative temperature difference, a slightly better prediction is observed for the OB approximation in this case. For the negative inclination case (Figures 11(*c*) and (*d*)), a similar behavior is observed so that in most of the isotherm surfaces, c_f values predicted by the

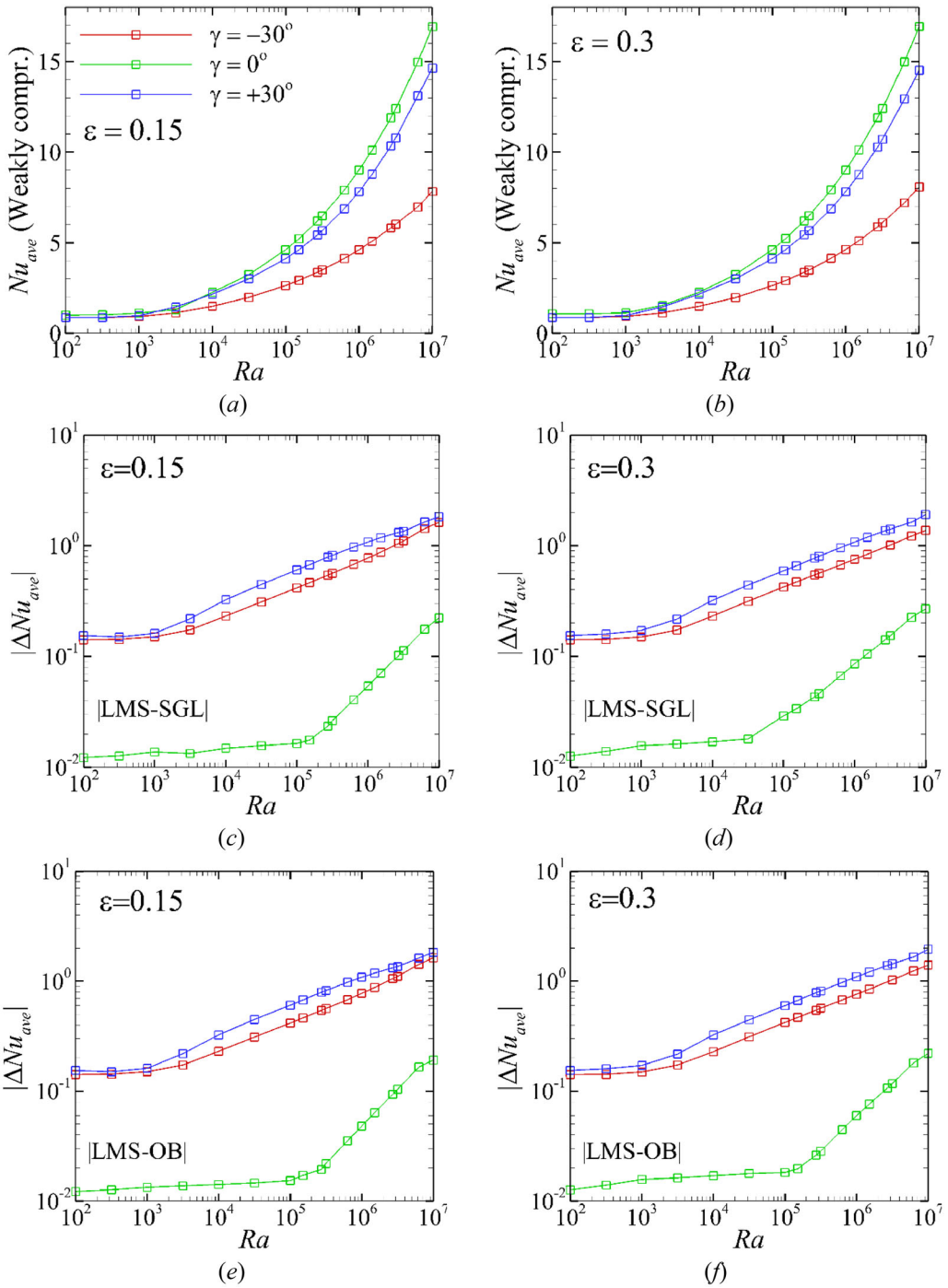

Figure 10. Average Nusselt number against Rayleigh number at $Pr = 1$ in square cavity with different inclination angles as stated: (*a*) $\varepsilon = 0.15$ and (*b*) $\varepsilon = 0.3$. Absolute average Nusselt number differences between the SGL and LMS approximations: (*c*) $\varepsilon = 0.15$ and (*d*) $\varepsilon = 0.3$. Absolute average Nusselt number differences between the OB and LMS approximations: (*e*) $\varepsilon = 0.15$ and (*f*) $\varepsilon = 0.3$.

incompressible approaches do not show a consider mismatch but as it can be seen, result under the SGL approximation deteriorate as the relative temperature difference is increased. For the

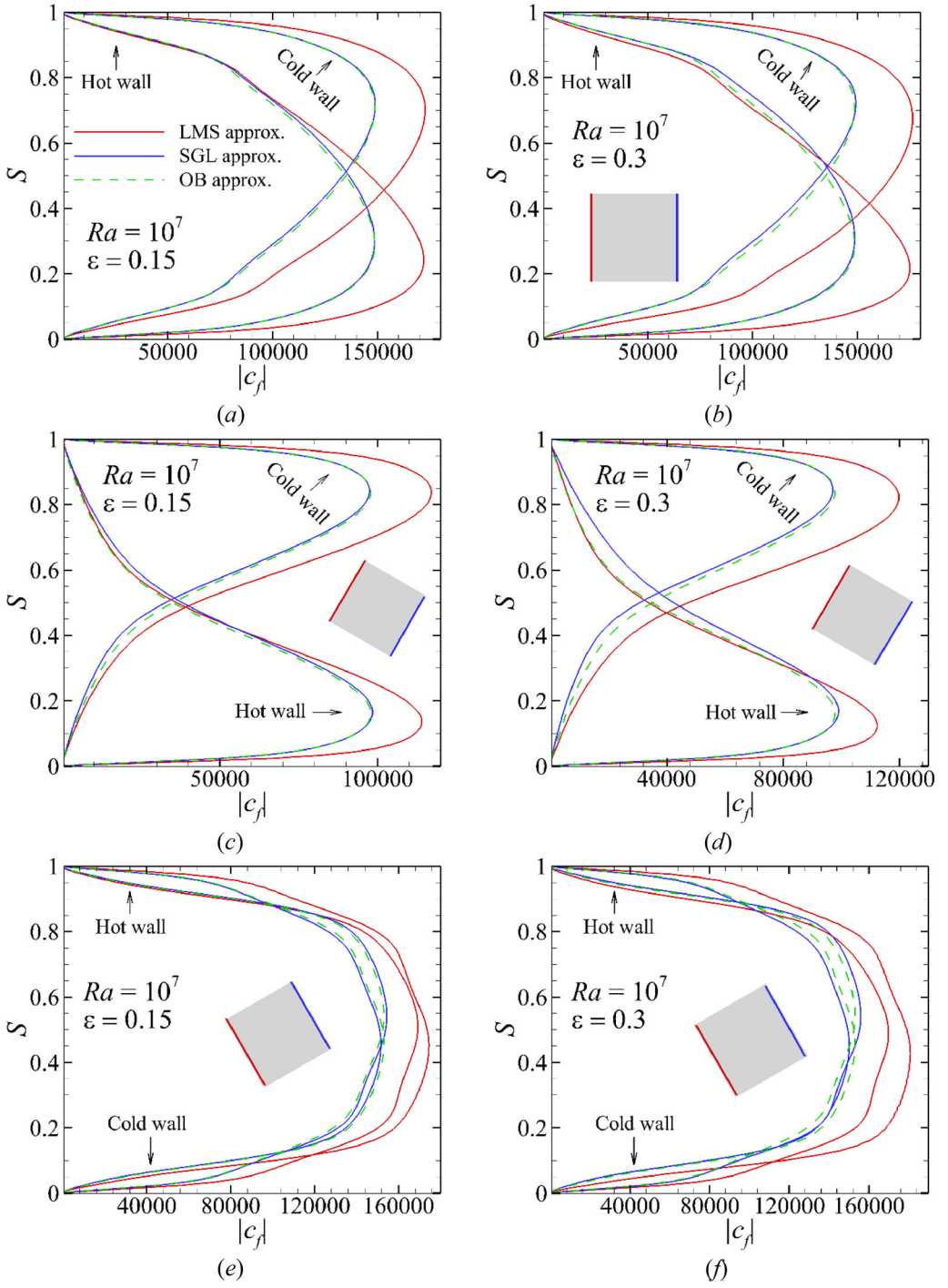

Figure 11. Local friction coefficient distributions along the isotherm walls at $Ra = 10^7$, $\varepsilon = 0.15$, and $\varepsilon = 0.3$: (*a, b*) zero inclination angle, (*c, d*) negative inclination angle ($\gamma = -30°$), and (*e, f*) positive inclination angle ($\gamma = 30°$).

positive inclination angle (Figures 11*e* and *f*), a better performance is observed for the SGL approach across the hot wall while the OB approximation works slightly better across the cold wall at both $\varepsilon = 0.15$ and 0.3.

6. Conclusion

In this study, a simplified and efficient form of the Gay-Lussac approach is proposed for non-Boussinesq treatment of the governing equations for the buoyancy driven flows. It is shown that removing density variations from the continuity equation brings no difference to the produced results compared to the traditional Gay-Lussac approach that is established based on considering density variations in any term of the governing equations in which density appears. This can be attributed to the density pre-factor to the velocity divergence in the mass conservation equation having no influence on the results in an incompressible framework. Results indicate that the proposed simplification reduces the computational cost of the traditional Gay-Lussac approach by 17% and 11% by applying the upwind and central schemes, respectively, while having no adverse impact on the convergence rate. Performance of the simplified Gay-Lussac approach is compared against the conventional Oberbeck—Boussinesq and weakly compressible approaches at high relative temperature differences in terms of the local and average Nusselt number and skin friction. In this respect, natural convection in square cavity with zero, negative and positive inclination angles is numerically simulated under the aforementioned approaches up to $Ra = 10^7$ at $Pr = 1$. Compared results show a considerable mismatch between the compressible and incompressible approaches at high relative temperature differences. Therefore, it is concluded the Gay-Lussac family of approaches require serious revisions to act more accurately than the Oberbeck—Boussinesq approximation at high relative temperature differences as an incompressible approach for buoyancy driven flows.

Deceleration of interest

No deceleration of interest.

Funding

This research was supported by the Australian Research Council through Discovery Project DP180102647. P. M. is supported by a Monash Graduate Scholarship and a Monash International Postgraduate Research Scholarship. The authors are also supported by time allocations on the National Computational Infrastructure (NCI) peak facility and the Pawsey Supercomputing Centre through NCMAS grants. NCI is supported by the Australian Government.

References

[1] J. Boussinesq, *Theorie Analytique de la Chaleur*. Paris: Gauthier-Villars, 1897.

[2] A. Oberbeck, "Ueber die Wärmeleitung der Flüssigkeiten bei Berücksichtigung der Strömungen infolge von Temperaturdifferenzen, "*Ann. Phys. Chem.*, vol. 243, no. 6, pp. 271–292, 1879. DOI: 10.1002/andp.18792430606.

[3] G. de Vahl Davis, "Natural convection of air in a square cavity, a benchmark numerical solution," *Int. J. Numer. Methods Fluids*, vol. 3, no. 3, pp. 249–264, 1983. DOI: 10.1002/fld.1650030305.

[4] I. V. Miroshnichenko and M. A. Sheremet, "Turbulent natural convection heat transfer in rectangular enclosures using experimental and numerical approaches: A review," *Renew. Sust. Energ. Rev.*, vol. 82, pp. 40–59, 2018. DOI: 10.1016/j.rser.2017.09.005.

[5] A. Mohamad, M. A. Sheremet, J. Taler and P. Ocłoń, "Natural convection in differentially heated enclosures subjected to variable temperature boundaries," *HFF*, vol. 29, no. 11, pp. 4130–4141, 2019. DOI: 10.1108/HFF-02-2019-0137.

[6] M. Sheremet, T. Groson and I. Pop, "MHD free convection flow in an inclined square cavity filled with both nanofluids and gyrotactic microorganisms," *HFF*, vol. 29, no. 12, pp. 4642–4659, 2019. DOI: 10.1108/HFF-03-2019-0264.

[7] D. C. Wan, B. S. V. Patnail and G. W. Wei, "A new benchmark quality solution for the buoyancy-driven cavity by discrete singular convolution," *Numer. Heat Transf. B*, vol. 40, pp. 199–228, 2001. DOI: 10.1080/104077901752379620.

[8] A. Ashrafizadeh and M. Nikfar, "On the numerical solution of generalized convection heat transfer problems via the method of proper closure equations–part II: Application to test problems," *Numer. Heat Transf. B*, vol. 70, no. 2, pp. 204–222, 2016. DOI: 10.1080/10407782.2016.1173467.

[9] S. C. Saha and M. M. K. Khan, "A review of natural convection and heat transfer in attic-shaped space," *Energy Buildings*, vol. 43, no. 10, pp. 2564–2571, 2011. DOI: 10.1016/j.enbuild.2011.06.020.

[10] O. M. Kamiyo, D. Angeli, G. S. Barozzi, M. W. Collins, V. O. S. Olunloyo and S. O. Talabi, "A comprehensive review of natural convection in triangular enclosures," *Appl. Mech. Rev.*, vol. 63, no. 6, pp. 060801, 2010. DOI: 10.1115/1.4004290.

[11] N. S. Bondareva, M. A. Sheremet, H. F. Oztop and N. Abu-Hamdeh, "Free convection in an open triangular cavity filled with a nanofluid under the effects of Brownian diffusion. thermophoresis and local heater," *J. Heat Transf. ASME*, vol. 140, no. 4, pp. 042502, 2018. DOI: 10.1115/1.4038192.

[12] M. A. Sheremet, I. Pop and A. Ishak, "Time-dependent natural convection of micropolar fluid in a wavy triangular cavity," *Int. J. Heat Mass Transf.*, vol. 105, pp. 610–622, 2017. DOI: 10.1016/j.ijheatmasstransfer.2016.09.044.

[13] Y. L. Wu, G. R. Liu and Y. T. Gu, "Application of Meshless Local Petrov-Galerkin (MLPG) Approach to Simulation of Incompressible Flow," *Numer. Heat Transf. B*, vol. 48, no. 5, pp. 459–475, 2005. DOI: 10.1080/10407790500324763.

[14] D. Angeli, G. S. Barozzi, M. W. Collins and O. M. Kamiyo, "A critical review of buoyancy-induced flow transitions in horizontal annuli," *Int. J. Therm. Sci.*, vol. 49, no. 12, pp. 2231–2241, 2010. DOI: 10.1016/j.ijthermalsci.2010.08.002.

[15] H. K. Dawood, H. A. Mohammed, and N. A. C. Sidik, K. M. Munisamy and M. A. Wahid, "Forced, natural and mixed-convection heat transfer and fluid flow in annulus: A review," *Int. Commun. Heat Mass Transf.*, vol. 62, pp. 45–47, 2015. DOI: 10.1016/j.icheatmasstransfer.2015.01.006.

[16] H. Paillere, C. Viozat, A. Kumbaro and I. Toumi, "Comparison of low Mach number models for natural convection problems," *Heat Mass Transf.*, vol. 36, no. 6, pp. 567–573, 2000. DOI: 10.1007/s002310000116.

[17] K. Szewc, J. Pozorski and A. Tanière, "Modelling of natural convection with Smoothed Particle Hydrodynamics: Non-Boussinesq formulation," *Int. J. Heat Mass Transf.*, vol. 54, no. 23-24, pp. 4807–4816, 2011. DOI: 10.1016/j.ijheatmasstransfer.2011.06.034.

[18] Q. Wang, S. Xia, R. Yan, D. Sun and Z. Wan, "Non-Oberbeck-Boussinesq effects due to large temperature differences in a differentially heated square cavity filled with air," *Int. J. Heat Mass Transf.*, vol. 128, pp. 479–491, 2019. DOI: 10.1016/j.ijheatmasstransfer.2018.06.079.

[19] J. K. Yuan, C. K. Ho and J. M. Christian, "Numerical simulation of natural convection in solar cavity receivers," *J. Solar Energy Eng.*, vol. 137, no. 3, pp. 031004, 2015. DOI: 10.1115/1.4029106.

[20] M. Niajalili, P. Mayeli, M. Naghashzadegan and A. H. Poshtiri, "Techno-economic feasibility of off-grid solar irrigation for a rice paddy in Guilan province in Iran: A case study," *Solar Energy*, vol. 150, pp. 546–557, 2017. DOI: 10.1016/j.solener.2017.05.012.

[21] J. Vierendeels, B. Merci and E. Dick, "Numerical study of natural convective heat transfer with large temperature differences," *Int. J. Numer. Methods HFF*, vol. 11, no. 4, pp. 329–341, 2001. DOI: 10.1108/09615530110389117.

[22] W. Fu, C. Li, C. Huang and J. Huang, "An investigation of a high temperature difference natural convection in a finite length channel without Bossinesq assumption," *Int. J. Heat Mass Trans.f*, vol. 52, no. 11-12, pp. 2571–2580, 2009. DOI: 10.1016/j.ijheatmasstransfer.2009.01.012.

[23] S. Busto, M. Tavelli, W. Boscheri and M. Dumbser, "Efficient high order accurate staggered semi-implicit discontinuous Galerkin methods for natural convection problems," *Comput. Fluids*, vol. 198, pp. 104399, 2020. DOI: 10.1016/j.compfluid.2019.104399.

[24] A. Bermúdez, S. Busto, M. Dumbser, J. L. Ferrín, L. Saavedra and M. E. Vázquez-Cendón, "A staggered semi-implicit hybrid FV/FE projection method for weakly compressible flows," *J. Comput. Phys.*, vol. 421, pp. 109743, 2020. DOI: 10.1016/j.jcp.2020.109743.

[25] S. Paolucci, "On the filtering of sound from the Navier-Stokes equations," Technical report, Sandia National Laboratories, no. 9, SAND 82-8257, 1982.

[26] J. Vierendeels, B. Merci and E. Dick, "A multigrid method for natural convective heat transfer with large temperature differences," *J. Comput. Appl. Math.*, vol. 168, no. 1-2, pp. 509–517, 2004. DOI: 10.1016/j.cam.2003.08.081.

[27] R. Becker and M. Braack, "Solution of a stationary benchmark problem for natural convection with large temperature difference," *Int. J. Therm. Sci.*, vol. 41, no. 5, pp. 428–439, 2002. DOI: 10.1016/S1290-0729(02)01335-2.

[28] T. Pesso and S. Piva, "Laminar natural convection in a square cavity: Low Prandtl numbers and large density differences," *Int. J. Heat Mass Transf.*, vol. 52, no. 3-4, pp. 1036–1043, 2009. DOI: 10.1016/j.ijheatmasstransfer.2008.07.005.

[29] J. M. Lopez, F. Marques and M. Avila, "The Boussinesq approximation in rapidly rotating flows," *J. Fluid Mech.*, vol. 737, pp. 56–77, 2013. DOI: 10.1017/jfm.2013.558.
[30] P. Mayeli and G. Sheard, "A new formulation for Boussinesq-type natural convection flows applied to the annulus cavity problem," *Int. J. Numer. Methods Fluids*, vol. 93, no. 3, pp. 683–702, 2021. DOI: 10.1002/fld.4904.
[31] P. Mayeli and G. Sheard, "Natural convection and entropy generation in square and skew cavities due to large temperature differences: A Gay-Lussac type vorticity stream-function approach," *Int. J. Numer. Methods Fluids*, vol. 93, no. 7, pp. 2396–2420, 2021. DOI: 10.1002/fld.4980.
[32] Y. R. Li, X. F. Yuan, C. M. Wu and Y. P. Hu, "Natural convection of water near its density maximum between horizontal cylinders," *Int. J. Heat Mass Transf.*, vol. 54, no. 11-12, pp. 2550–2559, 2011. DOI: 10.1016/j.ijheatmasstransfer.2011.02.006.
[33] E. A. Spiegel and G. Veronis, "On the Boussinesq approximation for a compressible fluid," *Astrophys. J.*, vol. 131, pp. 442–447, 1960. DOI: 10.1086/146849.
[34] J. A. Dutton and G. H. Fichtl, "Approximate equations of motion for gases and liquid," *J. Atmos. Sci.*, vol. 26, no. 2, pp. 241–254, 1969. DOI: 10.1175/1520-0469(1969)026<0241:AEOMFG>2.0.CO;2.
[35] D. D. Gray and A. Giorgini, "The validity of the Boussinesq approximation for liquids and gases," *Int. J. Heat Mass Transf.*, vol. 19, no. 5, pp. 545–551, 1976. DOI: 10.1016/0017-9310(76)90168-X.
[36] M. Pons and P. L. Quéré, "Modeling natural convection with the work of pressure-forces: A thermodynamic necessity," *Int. J. Numer. Methods HFF*, vol. 17, no. 3, pp. 322–332, 2007. DOI: 10.1108/09615530710730184.
[37] M. A. Leal, H. A. Machado and R. M. Cotta, "Integral transform solutions of transient natural convection in enclosures with variable fluid properties," *Int. J. Heat Mass Transf.*, vol. 43, no. 21, pp. 3977–3990, 2000. DOI: 10.1016/S0017-9310(00)00023-5.
[38] M. Souza, R. Miranda and H. Machado, "Natural convection in enclosures with variable fluid properties," *Int. J. Numer. Methods Heat Fluid Flow*, vol. 13, no. 8, pp. 1079–1096, 2003. DOI: 10.1108/09615530310501966.
[39] P. Mayeli, M. Nili-Ahmadabadi, M. R. Pirzadeh and P. Rahmani, "Determination of desired geometry by a novel extension of ball spine algorithm inverse method to conjugate heat transfer problems," *Comput. Fluids*, vol. 154, pp. 390–406, 2017. DOI: 10.1016/j.compfluid.2016.05.022.
[40] H. Hesami and P. Mayeli, "Development of the ball-spine algorithm for the shape optimization of ducts containing nanofluid," *Numer. Heat Transf. A*, vol. 70, no. 12, pp. 1371–1389, 2016. DOI: 10.1080/10407782.2016.1243976.
[41] M. Nikfar and P. Mayeli, "Surface shape design in different convection heat transfer problems via a novel coupled algorithm," *J. Heat Transf.-Trans. ASME*, vol. 140, no. 2, pp. 021702-1, 2018. DOI: 10.1115/1.4037581.
[42] P. Mayeli, and H. Hesami and M. H. D. F. Moghaddam, "Numerical investigation of the MHD forced convection and entropy generation in a straight duct with sinusoidal walls containing water-Al2O3 nanofluid," *Numer. Heat Transf. A*, vol. 71, no. 12, pp. 1371–1389, 2017. DOI: 10.1080/10407782.2016.1243976.
[43] P. Mayeli, H. Hesami, H. Besharati-Foumani and M. Niajalili, "Al_2O_3-Water nanofluid heat transfer and entropy generation in a ribbed channel with wavy wall in the presence of magnetic field," *Numer. Heat Transf. A*, vol. 73, no. 9, pp. 604–623, 2018. DOI: 10.1080/10407782.2018.1461494.
[44] A. Ashrafizadeh, B. Alinia and P. Mayeli, "A new co-located pressure-based discretization method for the numerical solution of incompressible Navier-Stokes equations," *Numer. Heat Transf. B*, vol. 67, no. 6, pp. 563–589, 2015. DOI: 10.1080/10407790.2014.992094.
[45] P. Mayeli and M. Nikfar, "Temperature identification of a heat source in conjugate heat transfer problems via an inverse analysis," *HFF*, vol. 29, no. 10, pp. 3994–4010, 2019. DOI: 10.1108/HFF-05-2018-0193.
[46] M. Nikfar, A. Ashrafizadeh and P. Mayeli, "Inverse shape design via a new physical-based iterative solution strategy," *Inverse Prob.Sci. Eng.*, vol. 23, no. 7, pp. 1138–1162, 2015. DOI: 10.1080/17415977.2014.973873.
[47] P. Mayeli, M. Nili-Ahmadabadi and H. Besharati-Foumani, "Inverse shape design for heat conduction problems via the ball spine algorithm," *Numer. Heat Transf. B*, vol. 69, no. 3, pp. 249–269, 2016. DOI: 10.1080/10407790.2015.1096690.
[48] P. L. Quéré, *et al.*, "Modelling of natural convection flows with large temperature differences: A benchmark problem for low Mach number solvers. Part 1. Reference solutions," *ESAIM M2AN*, vol. 39, no. 3, pp. 609–616, 2005. DOI: 10.1051/m2an:2005027.